FULL PAPER

Skin-Like Oxide Thin-Film Transistors for Transparent Displays

Han Eol Lee, Seungjun Kim, Jongbeom Ko, Hye-In Yeom, Chun-Won Byun, Seung Hyun Lee, Daniel J. Joe, Tae-Hong Im, Sang-Hee Ko Park,* and Keon Jae Lee*

Flexible transparent display is a promising candidate to visually communicate with each other in the future Internet of Things era. The flexible oxide thin-film transistors (TFTs) have attracted attention as a component for transparent display by its high performance and high transparency. The critical issue of flexible oxide TFTs for practical display applications, however, is the realization on transparent and flexible substrate without any damage and characteristic degradation. Here, the ultrathin, flexible, and transparent oxide TFTs for skin-like displays are demonstrated on an ultrathin flexible substrate using an inorganic-based laser liftoff process. In this way, skin-like ultrathin oxide TFTs are conformally attached onto various fabrics and human skin surface without any structural damage. Ultrathin flexible transparent oxide TFTs show high optical transparency of 83% and mobility of 40 cm² V⁻¹ s⁻¹. The skin-like oxide TFTs show reliable performance under the electrical/optical stress tests and mechanical bending tests due to advanced device materials and systematic mechanical designs. Moreover, skin-like oxide logic inverter circuits composed of *n*-channel metal oxide semiconductor TFTs on ultrathin, transparent polyethylene terephthalate film have been realized.

1. Introduction

Augmented reality (AR)[1] has attracted significant attention with the development of smart devices and the Internet of Things (IoT),[2] which can realize a hyperconnected society by collecting and exchanging bilateral information. Flexible transparent displays have been proposed as a powerful medium of visual communication that can be attached to anything, including the windows of vehicles and buildings, mirrors, and even eyeglasses for the efficient use of space. Flexible

active-matrix organic light-emitting diode (f-AMOLED) is potentially strong candidates for use in these devices, as they have high optical transparency exceeding 80%[3] with outstanding performance capabilities, as exemplified by their rapid refresh rates, short response time, and low power consumption levels.[4,5]

The backplane of oxide thin-film transistors (TFTs) has been spotlighted as a switching and driving component for transparent f-AMOLED due to its high mobility,[6] low leakage current,[7] and high transparency.[8] Several research groups have reported various approaches to create flexible oxide TFTs by means of direct deposition onto plastics,[9] solution-coating methods,[10,11] and with composite-based nanomaterials.[12] These methods, however, are associated with the fact that the oxide TFTs on flexible substrates exhibit insufficient performance levels and low production yields compared to those on conventional glass substrates, owing to the inherent issues of high-temperature compatibility[13] or their yellowish plastic color.[14] Our group has recently developed high-performance flexible one selector-one memristor (1S-1M) devices utilizing an inorganic-based laser liftoff (ILLO) process,[15] an advanced exfoliation process for transferring only inorganic thin-film devices fabricated on a rigid substrate onto a large-area plastic substrate. While the application of flexible high-density memory has been investigated, the ILLO process has not been exploited for display technology, where the largest flexible electronic market exists.

Recently, skin-like electronics (thickness <5 μm, transmittance >80%) that can be conformally attached onto any type of curvilinear surface have been reported for human/machine interfaces, wearable technologies, and biomedical applications.[16,17] Despite the demonstrations of ultrathin electronics such as organic thin-film transistors[18] and strain sensors,[19–21] the skin-like display remains as a challenge to achieve next-generation imperceptible displays or display of things.

Here, we realize high-performance, skin-like, transparent oxide TFT arrays using the ILLO process. The 50 × 50 indium zinc oxide (IZO) TFT array, fabricated with a laser-reactive exfoliation layer on a rigid glass substrate, was successfully transferred onto an ultrathin flexible substrate (4 um thickness). After irradiation by an excimer laser through the backside of the

H. E. Lee, Dr. S. Kim, J. B. Ko, H.-I. Yeom, S. H. Lee,
Dr. D. J. Joe, T.-H. Im, Prof. S.-H. K. Park, Prof. K. J. Lee
Department of Materials Science and Engineering
Korea Advanced Institute of Science
and Technology (KAIST)
291 Daehak-ro, Yuseong-gu
Daejeon 34141, Republic of Korea
E-mail: shkp@kaist.ac.kr; keonlee@kaist.ac.kr
C.-W. Byun
Information & Communications Core Technology Research Laboratory
Electronics and Telecommunications Research Institute (ETRI)
218 Gajeong-ro, Yuseong-gu, Daejeon 34129, Republic of Korea

www.MaterialsViews.com

ADVANCED
FUNCTIONAL
MATERIALS
www.afm-journal.de

FULL PAPER

glass substrate onto the exfoliation layer, only the upper inorganic oxide TFT layers were exfoliated from the bulk mother glass substrate without structural damage. The skin-like oxide TFT arrays were conformally and stably attached to fabric and to human skin by utilizing a sophisticated theoretical design and with optimization by the finite-element method (FEM) to avoid thermal and structural damage during the ILLO process. The skin-like transparent oxide TFTs exhibited an excellent effective mobility of ≈40 cm^2 V^{-1} s^{-1}. Furthermore, the flexible oxide TFT arrays showed superior optical/electrical stability for active matrix display applications; the threshold voltage shifted less than −1 V under positive bias temperature illumination stress (PBTIS) and −4 V under negative bias temperature illumination stress (NBTIS). Our skin-like IZO TFTs reliably operated for 5000 repeated bending/unbending cycles without serious degradation at a bending radius of 7.5 mm. Finally, we devised a skin-like oxide logic inverter composed of n-channel metal oxide semiconductor (NMOS) TFTs on ultrathin, transparent polyethylene terephthalate (PET) film.

2. Results and Discussion

Figure 1a shows a schematic illustration of the skin-like transparent oxide TFT array on an ultrathin plastic substrate. The skin-like oxide TFT fabrication process is as follows. Prior to the construction of the oxide TFT array, a hydrogenated amorphous silicon (a-Si:H, thickness, 50 nm) and a silicon oxide (SiO$_2$) layer were grown by plasma-enhanced chemical vapor deposition (PECVD) on a glass substrate (Corning Lotus Display Glass, thickness = 700 μm) as an exfoliation layer and a buffer layer, respectively. The 50 × 50 oxide TFT arrays, which consist of high-quality oxide thin films annealed at 350 °C, were fabricated on the buffer layer, as illustrated in the active-matrix circuit diagram shown in the inset of Figure 1a. Each active-matrix pixel unit on the glass substrate was composed of two oxide TFTs and a capacitor as the switching and driving components with a rapid response, interconnected by Gate, Data, and V_{DD} lines. To eliminate the sacrificial glass substrate from the oxide TFT backplane, an XeCl excimer laser with a wavelength of 308 nm, widely commercialized in low temperature polycrystalline silicon,[22] was irradiated from the backside of a transparent glass substrate (transmittance over 73% at a wavelength of 308 nm). The upper oxide TFT layers were detached from the bulk glass substrate by reducing the adhesion between the laser-reacted a-Si:H layer and the bulk mother substrate, thereby facilitating the transfer onto the ultrathin PET film. (Detailed information about the entire fabrication process can be found in the Supporting Information, including a summary of the fabrication process of the oxide TFT array on a flexible substrate, shown in Figure S1.)

Figure 1b displays cross-sectional transmission electron microscopy (TEM) images of the high-performance IZO TFT on the glass mother substrate before the ILLO process. The upper inset shows a high-resolution TEM (HRTEM) image of oxide device layers. An indium tin oxide (ITO) gate layer was patterned by direct current (DC) sputtering and a standard photolithography process on a glass substrate. A gate insulator (GI) consisting of aluminum oxide (Al$_2$O$_3$) was grown by atomic

layer deposition (ALD) at 150 °C. The same experimental conditions used with the gate layer were applied to the ITO thin film used for the source/drain layer. Amorphous IZO (20 nm thick) as an active layer was deposited by radio-frequency (RF) sputtering (Figure S5, Supporting Information). The SiO$_2$ passivation layer was grown by PECVD at 300 °C to prevent water and oxygen gas from degrading the oxide TFTs. By means of energy dispersive spectrometer (EDS) elemental mapping, as shown in the lower inset of Figure 1b, we clearly confirmed the constituent elements of the pure oxide TFT layers. Figure 1c presents a magnified optical microscopic image of the 50 × 50 oxide TFT array transferred onto an ultrathin PET substrate (4 μm thick). The active-matrix array, which consists of a switching TFT (W/L = 40/20 μm), a driving TFT (W/L = 160/20 μm), and a capacitor, was attached to the skin-like polymer film without mechanical damages (i.e., wrinkling of cracking). After the ILLO transfer process, the used sacrificial substrates may be reutilized multiple times,[15] demonstrating the good economic advantages of the ILLO process. The skin-like transparent oxide TFT array can easily be attached to human skin with biocompatible glue, evenly covering the wrist area of the blood vessels, as shown in Figure 1d. Figure 1e displays skin-like IZO TFTs attached to the surface of a jumper sleeve to demonstrate wearable applications without wrinkling and delamination during arm movements. Moreover, it is extremely hard to distinguish the skin-like oxide devices from the background object such as human skin or cloth.

To interpret the exfoliation phenomena,[23,24] we theoretically calculated the temperature distribution of the laser-reactive layer using FEM and experimentally analyzed its detaching mechanism. The ILLO process is based on melting,[25] dissociation,[26] or vaporization[27] of an optical-reactive layer when it interacts with a high-energy laser. Upon laser irradiation, the temperature of the exfoliation layer instantaneously reaches thousands of kelvin,[27] resulting in laser-induced thermal damages to active device layer. To protect the oxide TFT layers from thermal damage induced by heat diffusion, the laser energy density and the thickness of the buffer oxide layer should be carefully optimized.[28] **Figure 2**a shows the simulated temperature distribution in FEM heat flux mode during the ILLO process. The heat flux through the entire device was solved by the heat transfer equation

$$\rho C \frac{\partial T}{\partial t} - \nabla(k \nabla T) = Q \tag{1}$$

where ρ is the density, C is the specific heat, k is the thermal conductivity, and Q is the total heat caused by laser irradiation. Given that a-Si:H thin film has a specific absorption and reflection rate at a wavelength of 308 nm, the laser heat source can be redefined by the following equation

$$Q(x, y) = (1 - R) I_0 \alpha_C e^{-\alpha_C y} \tag{2}$$

Here, I_0 denotes the intensity of the laser, R is the reflectance, and α_C is the absorption coefficient of a-Si:H (Figure S6, Supporting Information). According to the calculation results, while the temperature of the a-Si:H layer with a laser density of 460 mJ cm^{-2} rises instantly up to 3231 K, the buffer oxide
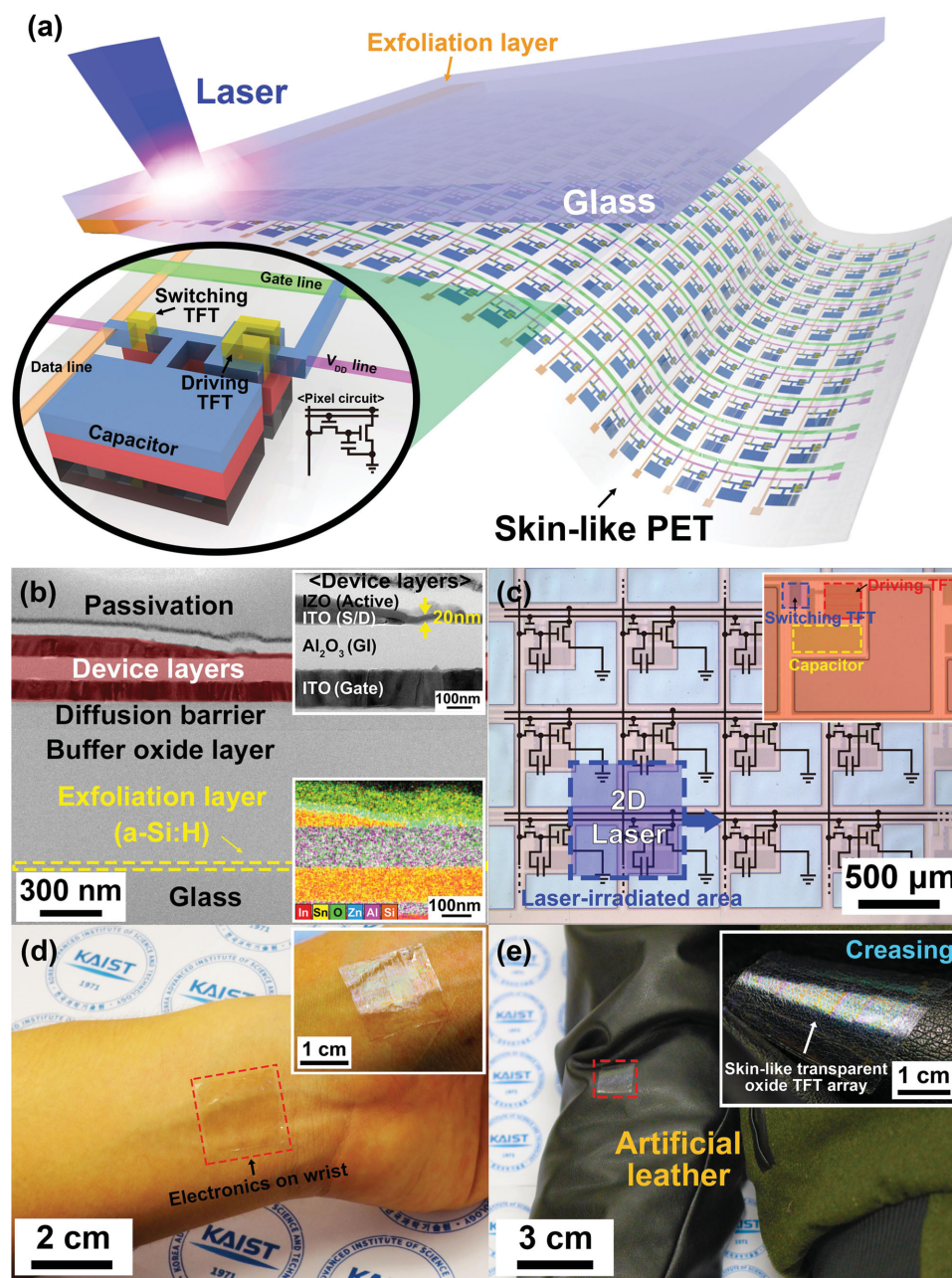
Figure 1. a) Schematic illustrations of a skin-like oxide TFT array for transparent display via the ILLO fabrication process, consisting of a switching TFT, a driving TFT, and a capacitor. The inset shows an active-matrix pixel unit with a circuit diagram. b) A cross-sectional TEM image of the entire oxide TFT on a glass substrate. The upper inset shows a cross-sectional bright-field TEM image of an oxide TFT between the buffer oxide layer and the passivation layer. The lower inset shows the EDS elemental mapping results. c) A magnified optical microscopy image of the active-matrix oxide TFT array. The inset shows a unit pixel of the array. d) A photograph of a skin-like oxide TFT array attached to a human wrist. The inset is a picture of a transparent oxide TFT array reflecting white lamplight. e) A picture of a skin-like oxide TFT array attached to the sleeve of a jumper. The inset shows an enlarged photograph of the skin-like transparent oxide TFT array on creased cloth.

layer with a thickness of 1 µm sufficiently protects the oxide TFTs from thermal laser damage. Figure 2b presents the simulated temperature profile versus the entire vertical structure after laser irradiation. During a laser duration time of 30 ns, the interface temperature between the a-Si:H and the buffer oxide layers increased to 3231 K, then distributed throughout the entire structure by conductive heat transfer. As shown in

the temperature profile versus vertical position within an ultra-short time, the influence of the nanosecond laser on the active oxide TFT layer is negligible due to its extremely short pulse and sufficient buffer oxide thickness. Figure 2c shows an optical microscopy image of the a-Si:H film on the remaining glass substrate after the ILLO process. We confirmed the presence of repetitive rectangular patterns on the surface of the sacrificial
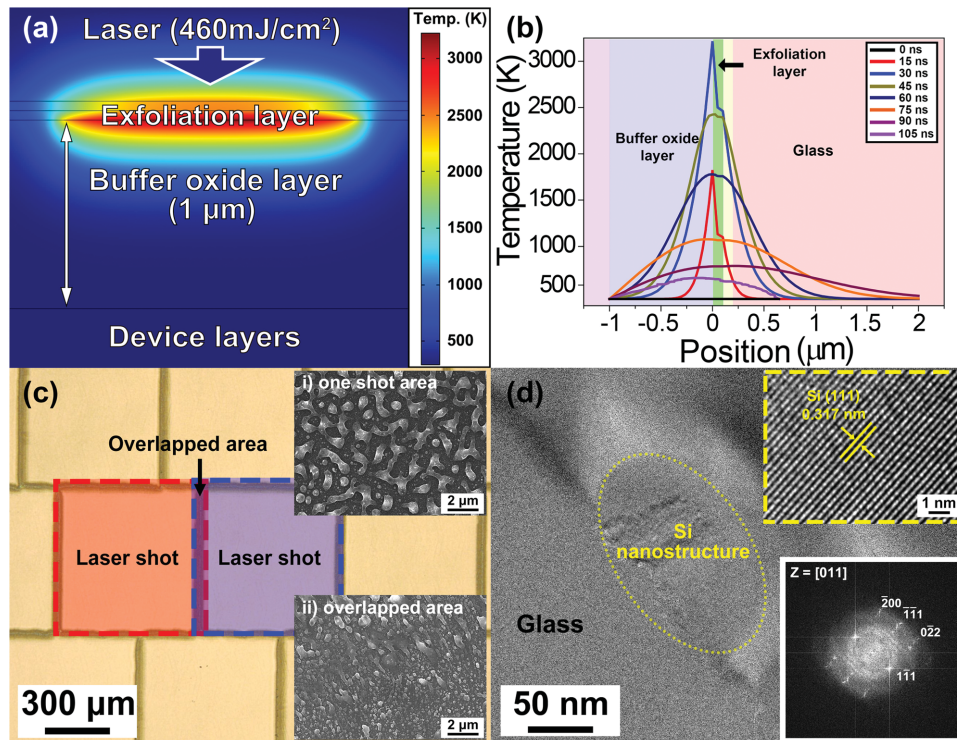
Figure 2. a) Heat distribution in an FEM simulation when an excimer laser with 460 mJ cm^{-2} is irradiated onto the exfoliation layer through the backside of a glass substrate. b) Calculated temperature profile as a function of the overall structure dimensions (in the z-direction). The graphs show that it takes nearly 105 ns for the heated device to cool down after the laser exposure. The time changes from zero to 105 ns until the entire heated structure cools down to room temperature. c) Optical microscopy image of rectangular patterns formed on a sacrificial glass substrate after the ILLO process. The insets display SEM images of the agglomerated Si nanostructures in the area exposed to the laser. d) TEM analysis results of the Si nanostructure formed on the sacrificial glass substrate. The upper inset shows a cross-sectional HRTEM image of the Si nanostructure. The lower inset is a fast Fourier transform image of the Si lattice in the HRTEM image.

substrate, as created by 2D laser shots (625 × 625 μm^2) with an overlapped length of 20 μm at 10 Hz of laser shot frequency. After the XeCl laser was exposed to the a-Si:H layer, the optical-reactive film melted and easily released hydrogen gas. The released hydrogen gas, with volume expansion, reduced the adhesion between the glass substrate and the a-Si:H film,[29,30] resulting in detachment of all device layers from the sacrificial substrate.[31] The insets present the scanning electron microscopy (SEM) images of the laser irradiated area. The SEM images show the randomly assembled Si nanostructures on the remaining glass substrate. In-depth investigation of the a-Si:H film surface by means of HRTEM and EDS analyses reveals that random Si agglomerations formed on the glass substrate, as in Figure 2d. A high-magnification image shows the crystalline lattice of the Si nanostructure with a d-spacing value of 0.317 nm along the [111] direction (the upper inset in Figure 2d). The lower inset describes the corresponding fast Fourier transform pattern of the crystalline Si. Upon irradiation with the laser, the a-Si:H film was heated over the Si melting point, subsequently transforming from the amorphous to the crystalline phase.[32] The EDS results also indicate that the Si nanostructures were agglomerated on the sacrificial glass substrate after the ILLO process (Figure S8, Supporting Information). It appears that the assembled Si nanostructures weakened the adhesion between the buffer oxide layer and the glass substrate by reducing the contact area. The agglomerated Si

nanostructures can be easily removed by SF$_6$-based inductively coupled plasma dry etching.[15]

Figure 3a depicts a cross-sectional schematic illustration of an IZO TFT unit cell on a flexible PET substrate. We fabricated a bottom gate structure of the IZO TFT, which offers the advantage of a simple fabrication process compared to a top-gated TFT.[33] The optical characteristics of the transparent IZO TFT are shown in terms of the UV-visible transmittance spectra in Figure 3b. In this figure, the flexible IZO TFT array on the transparent PET substrate showed outstanding average transmittance of >83% in the visible light region (wavelengths of 400–700 nm) as compared to the 88% transmittance of the PET substrate.[34–36] The insets in Figure 3b and Figure S9 (Supporting Information) indicate the high transparency of the flexible IZO TFT, clearly presenting the emblem behind the wide-bandgap IZO TFT on the plastic substrate.[37]

The transfer characteristics (I_{DS}–V_{GS}) of an IZO TFT unit cell on a glass and flexible substrate are displayed in Figure 3c on a semi-logarithmic scale, indicating a subthreshold swing (SS) of 168 mV dec^{-1} and a drain current on/off ratio of ≈8 × 10^7. It is clearly demonstrated that both n-type IZO TFTs effectively show no differences in their transfer characteristics during the ILLO process. The right inset in Figure 3c shows a plot of the field-effect mobility (μ_{FE}) versus the gate bias (V_{GS} at V_D = 0.1 V. The effective μ_{FE} value is determined to be 40.1 cm^2 V^{-1} s^{-1} on the glass substrate and 39.5 cm^2 V^{-1} s^{-1} on the plastic substrate
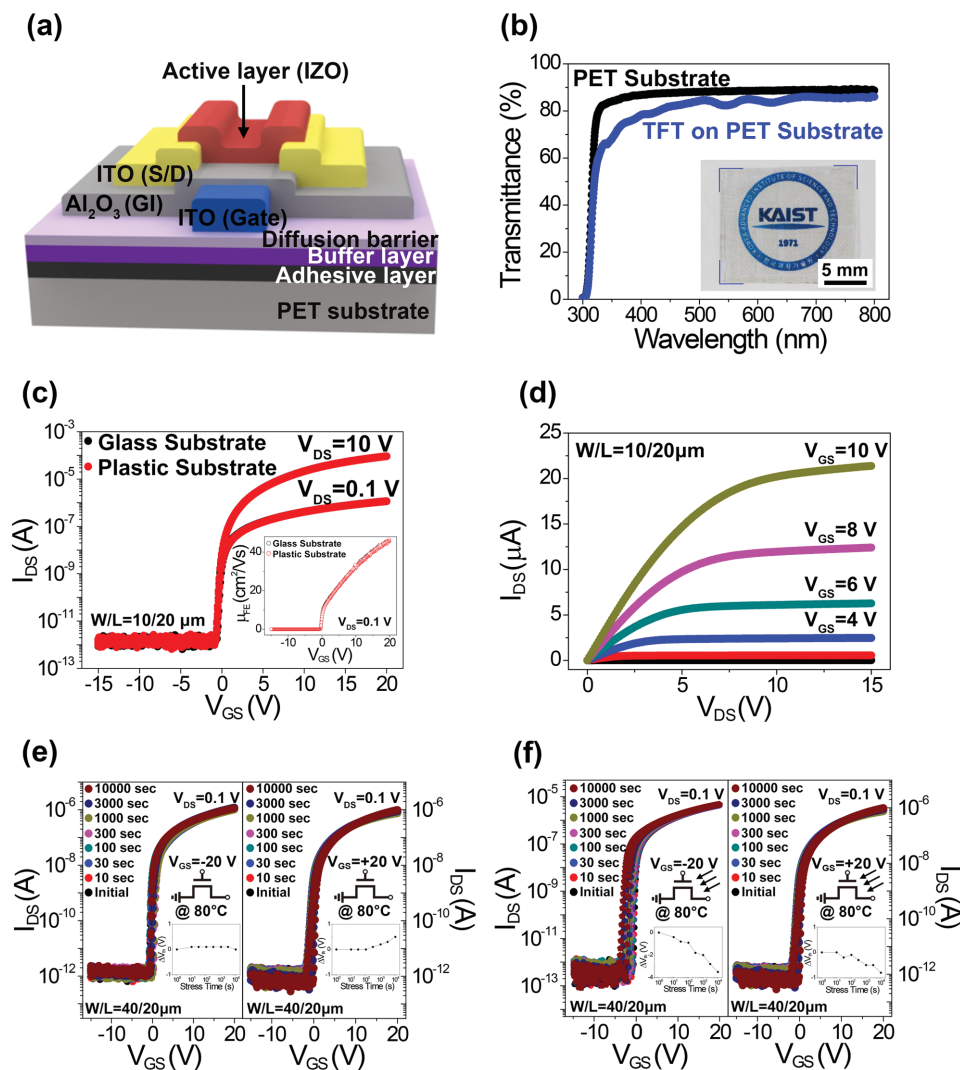
Figure 3. a) 3D schematic illustration of a unit cell of an IZO TFT based on an IZO active layer. b) The transmittance spectra of the transparent IZO TFT array and commercialized transparent PET film. The inset shows an optical image of an oxide TFT array on skin-like plastic film as marked by the blue lines. c) Transfer characteristics on a semi-logarithmic scale of an IZO TFT. The lower inset shows μ_{FE} as a function of V_{GS} at a drain voltage of 0.1 V. d) Output characteristic of the IZO TFT with V_{GS} varying from 0 to 10 V in 2 V steps. Transfer characteristics of the IZO TFT on a plastic substrate (e) under NBTS (left) and PBTS (right) conditions, and (f) under NBTIS (left) and PBTIS (right) conditions for 10 000 s. Each inset shows the change of the threshold voltage as a function of the applied stress time.

at V_{GS} = 15 V. Figure 3d presents the output characteristics (I_{DS}−V_{DS}) of an n-type IZO TFT on a flexible substrate with six different values of V_{GS}, exhibiting the linearity of the drain current (I_{DS}) in the low-V_{DS} region (triode region) and its saturation in the high-V_{DS} region. The transferred flexible oxide TFTs displayed suitable gate modulation with I_{DS} proportional to V_{GS}. As compared to the findings in previous studies,[11,36,38] the excellent electrical characteristics of our flexible oxide TFTs come from the ILLO process, which provides high stability even at high temperatures exceeding 500 °C.[27]

The oxide TFTs of commercial displays are generally affected by prolonged negative and positive gate voltage stress,[39] and by the temperature,[40] and illumination,[41,42] causing a threshold voltage shift and reduced lifetimes. In order to confirm the practical capability of our flexible transparent oxide TFT, we undertook various stability tests such as negative bias

temperature stress (NBTS), positive bias temperature stress (PBTS), NBTIS, and PBTIS tests. Figure 3e shows the NBTS (left) and PBTS (right) results when V_{GS} = ±20 V and V_{DS} = 0.1 V at 80 °C. After external stress of 10 000 s, negligible changes of the threshold voltage (ΔV_{th}) were observed in the NBTS tests, because minority positive-donors that related with the oxygen vacancies are trapped at the interface between the GI and the active layer (Figure S12a, Supporting Information). In case of PBTS assessments, however, ΔV_{th} = 0.8 V of our IZO TFT stems from electron trapping near the interface between the GI and the active layer (Figure S12b, Supporting Information).[43] In the PBTS, it has been well known that the oxygen plasma causes the damages on the GI surface during the oxide thin film deposition,[44] resulting in parallel positive V_{th} shifts without a significant change in the SS.[45] Under normal AMOLED operation, the autonomous illumination

Materials
Views
www.MaterialsViews.com

ADVANCED
FUNCTIONAL
MATERIALS
www.afm-journal.de

FULL PAPER

effect is important;[46] thus, the light-susceptibility characteristics of our oxide TFTs should be investigated in NBTIS and PBTIS tests. In Figure 3f, the oxide TFTs were optically and electrically stressed under $V_{GS} = \pm 20$ V, $V_{DS} = 0.1$ V and light density with luminous intensity of 500 cd m^{-2}[47,48] at 80 °C. 500 cd m^{-2} is currently known to be the maximum luminance exposed by smart phones (≈ 300 cd m^{-2} for normal operation). After the flexible TFTs were exposed to light for 10 000 s, ΔV_{th} values of -3.7 V in NBTIS and -0.8 V in PBTIS were observed. Under dark stress conditions, the value ΔV_{th} was extremely low for all of the NBS, NBTS, due to negligible density of the generated hole carriers.[49] In NBTIS stress tests, the transparent all-oxide TFTs typically show enormous negative V_{th} shifts which are caused by electron depletion and photogenerated holes[50,51] trapping at the interface of the GI/active layer.[52,53] In the case of PBTIS stress test here, the transparent all-oxide TFTs commonly exhibit insignificant negative ΔV_{th} values caused by the compensation of the illumination-induced negative V_{th} shift and the positive V_{th} shift which originated from the charge trapping.[54] As presented in Figure 3f, our flexible transparent oxide TFTs showed the valid results based on the considerations above reasons in the diverse stress tests conducted here.[55]

The mechanical stability of the flexible oxide TFTs was examined in bending tests with various bending curvature radii and cycles, as shown in **Figure 4**a,b. In Figure 4a, the bent oxide TFTs result in typical transfer graphs on a curved PDMS mold (left: horizontal bending from the channel direction,

right: vertical bending from the channel direction). Despite the diverse curvature radii and bending directions, ΔV_{th} shifted only by ≈ -0.4 V on a half-cylindrical PDMS mold. SS values showed no significant changes directly related to the bending directions or bending radii (Table S2, Supporting Information). Figure 4b presents the outstanding mechanical durability of the oxide TFTs at a curvature radius of 7.5 mm with luminous intensity of 500 cd m^{-2} which is the real operating condition of flexible display.[44,45] ΔV_{th} shifted by -0.4 V during the repetitive bending of 5000 cycles. This remarkable mechanical stability is attributed to the polymer encapsulation layer on the top of devices, which can be explained in the form of a mechanical neutral plain given the following equation[56]

$$h_{neutral} = \sum_{i=1}^{N} \overline{E}_i h_i \left(\sum_{j=1}^{i} h_j - \frac{h_i}{2} \right) \bigg/ \sum_{i=1}^{N} \overline{E}_i h_i \qquad (3)$$

Here, $\overline{E}_i$ is the effective Young's modulus and h_i is the thickness of the ith layer. According to the calculated results, the mechanical neutral plane is located at a thickness of nearly 6.4 μm below the top surface. Because the epoxy encapsulation layer coated onto the top of the oxide TFTs has a thickness of ≈ 6 μm, the stress-free region is located at the center of the TFT device layers (see the Supporting Information for details.) With this mechanically neutral design of our ultrathin oxide TFTs, we could not find any mechanical damage in the oxide layers under severe bending conditions.[57–59]
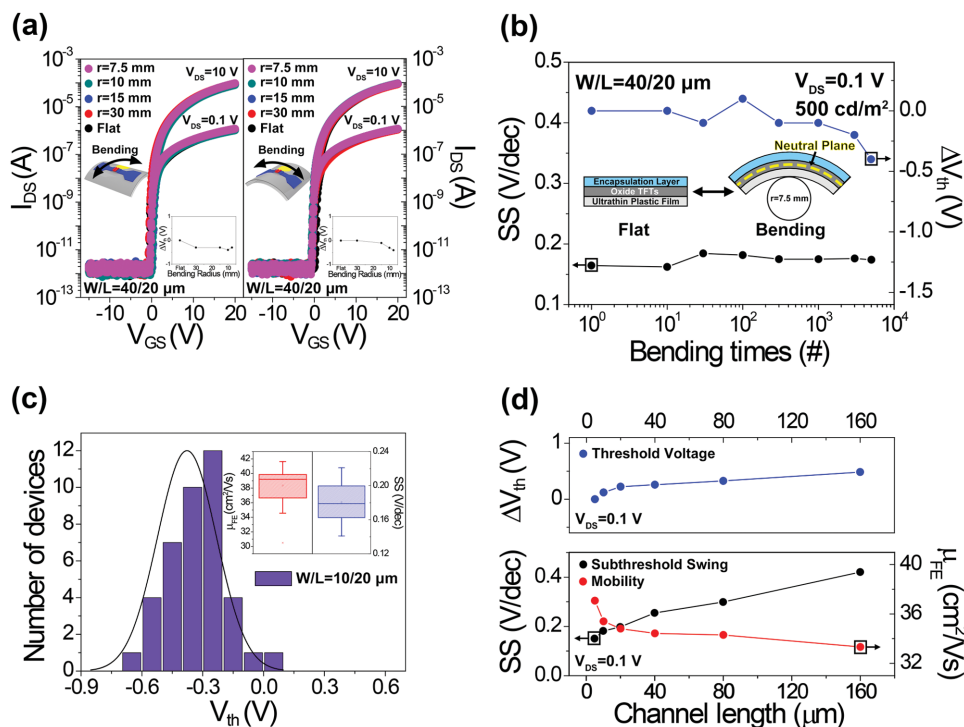

Figure 4. a) Transfer characteristics of an IZO TFT on a half-cylindrical PDMS mold with various radii in the horizontal (left) and vertical (right) bending directions. The insets display the changes of the threshold voltage. b) Bending fatigue test results of the subthreshold swing and changes of ΔV_{th} for the IZO TFT with 5000 continuous bending/unbending cycles at a bending curvature radius of 7.5 mm with luminous intensity of 500 cd m^{-2}. c) Distribution histogram with a threshold voltage of 40 of TFT devices on a flexible plastic substrate. The upper inset shows box-whisker plots of the field-effect mobility and subthreshold swing. d) Oxide TFT performance parameters as a function of the channel length on a flexible plastic substrate with a channel width of 20 μm (blue: change of the threshold voltage, black: subthreshold swing, red: the effective field-effect mobility).

To test the uniformity of the oxide TFTs, the electrical characteristics of 40 individual n-type IZO TFTs on a plastic substrate were measured, presenting comparatively uniform outcomes. As shown in Figure 4c, a statistical histogram of V_{th} expresses the best-fit Gaussian distribution, showing that 72.5% of the devices have a V_{th} value which ranges from −0.8 to −0.6 V. The box-whisker plots shown in the inset of Figure 4c present a narrow distribution with an average μ_{FE} of 38.5 cm^2 V^{-1} s^{-1} and with a SS of 180 mV dec^{-1}. Figure 4d compares the electrical parameters of the oxide TFTs as a function of different channel lengths (L) with a specific channel width (W). In general, V_{th} and SS are proportional to the channel length, while μ_{FE} is inversely proportional to the channel length.[60] The oxygen vacancies generated near the interface between the source/drain and active layer during the high temperature annealing can be diffused into the channel, resulting in decrease of the effective channel length than the mask design and cause an overestimation of μ_{FE}.[61] ΔV_{th} was also influenced due to the increased carrier amounts by diffusion of oxygen vacancy from the source/drain to the active layer.[62] However, other origin also should be investigated for the full analysis since the diffusion length of oxygen vacancy would not be longer than 40 μm. Although it is unclear why the SS is proportional to the channel length, we speculate that the compressive stress within each oxide TFT layer is the predominant cause of the change in the bandgap and the density of states.[63]

Finally, skin-like oxide logic inverter circuits were characterized on a transparent PET film with a thickness of 4 μm. **Figure 5**a shows a magnified optical image and a circuit diagram of the enhancement-load NMOS inverter,[64] which consists of the load and drive transistors. The load and drive TFTs have a channel width of 50 and 100 μm, respectively, with an identical channel length of 10 μm. Figure 5b displays the typical static voltage transfer characteristics (VTC) for the enhancement-load NMOS inverter setting supply voltage (V_{DD}) from 0 to 5 V on ultrathin plastic substrates. There were no significant changes of V_{out} between the glass and skin-like substrates. As shown in Figure 5c, the static VTC of the flexible inverter circuits was slightly shifted to the right with a decrease in the bending curvature radii at V_{DD} of 1 V. These inverter circuits exhibited a voltage gain of about 1.1, as calculated from $-dV_{out}/dV_{in}$ (the right inset of Figure 5c). Lastly, we evaluated the dynamic responses of the flexible inverter circuit on a flat and a half-cylindrical mold with a bending curvature radius of 7.5 mm (see Figure 5d). Flexible inverter circuits were driven with a constant V_{DD} of 5 V and an input voltage (V_{in}) of 100 Hz with a rectangular waveform ranging from 0 to 5 V. The measured rise (T_r) and fall times (T_f) of V_{out} were 30 and 54 μs on the skin-like film, respectively, proving the excellent mechanical/electrical stability of the developed devices. The electrical characteristics of flexible oxide inverters were identical to the predicted results by PSPICE circuit simulation (Figure S15, Supporting
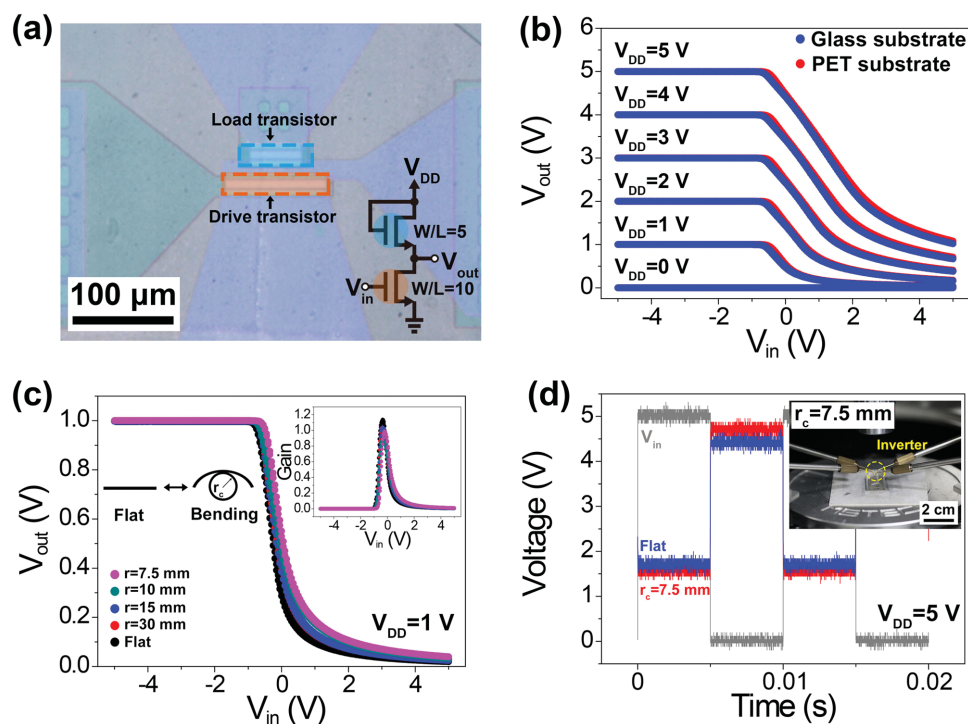

Figure 5. a) A magnified optical microscopy image and schematic circuit diagram of an IZO-based enhancement-load NMOS inverter. b) Static transfer characteristics of the NMOS inverter as a function of the input voltage. The blue lines indicate the characteristics on a glass substrate and the red lines indicate those on a skin-like PET substrate. c) Output characteristics of NMOS inverters with V_{DD} = 1 V under various bending states. The inset shows the voltage gain of the NMOS inverter at diverse bending curvature radii. d) Dynamic operation of the NMOS inverter circuit. An AC input voltage of 5 V with a 100 Hz rectangular waveform was applied to the inverter using a function generator. The gray line shows the input voltage, the blue line shows the output voltage in a flat state, and the red line shows the output voltage of the flexible inverter on the curved PDMS mold. The right inset displays a photograph of the measurement process in a bent state.

Information). These findings with the oxide inverter imply that our ultrathin oxide TFTs in conjunction with the ILLO process can be successfully applied to electronic logic circuits.

3. Conclusions

In conclusion, we have demonstrated high-performance, skin-like, transparent oxide TFT arrays using the ILLO process. The high-performance oxide TFTs were transferred from a glass substrate onto an ultrathin polymer film with a thickness of 4 μm for attachment to human skin and wearable clothes by a laser-based delamination process. FEM simulations and surface analyses (TEM, SEM, and EDS) were utilized to optimize the sophisticated material, structure, and thermal design of the transfer protocol. The flexible transparent oxide TFTs demonstrated outstanding characteristics, with mobility as high as 38.5 cm^2 V^{-1} s^{-1}, an SS of 180 mV dec^{-1}, an on/off ratio of ≈8 × 10^7, a threshold voltage of −0.3 V, and optical transmittance of 83% in the visible light region. The excellent stress stability of the skin-like transparent oxide TFTs was confirmed by NBTIS and PBTIS tests under direct illumination. The flexible oxide TFTs also showed mechanical durability up to 5000 continuous bending/unbending cycles. The NMOS oxide inverter circuits on the ultrathin plastics exhibited superior static and dynamic electrical characteristics with bending curvature radii of 7.5 mm. Therefore, the ultrathin, flexible, and transparent oxide TFTs using the ILLO process could be used to realize a prosperous approach for the development and commercialization of skin-like AMOLEDs. We are currently investigating ultrathin transparent AMOLEDs using high performance oxide TFT and ILLO technologies to the realization of AR for coming IoT era.

4. Experimental Section

Fabrication of the IZO TFT: ITO as the gate layer was grown by DC sputtering with an ambient pressure (Ar 10 sccm, O$_2$ 0.6 sccm) of 0.67 mTorr Ar/O$_2$ at room temperature and was patterned by photolithography and a wet etching process on a bulk glass substrate. Afterward, a GI of Al$_2$O$_3$ was deposited by ALD at 150 °C. The same experimental conditions were used for the ITO thin film as a sputtering source/drain layer. The active layer of IZO was grown by RF sputtering under an ambient pressure (Ar 6.4 sccm, O$_2$ 2.9 sccm) of 0.65 mTorr Ar/O$_2$ at room temperature. Finally, all devices were passivated by a 100 nm thick SiO$_2$ at 300 °C to protect the vulnerable oxide films from oxygen and water vapor.

Electrical Measurements: The electrical characteristics of the IZO TFTs and NMOS inverter circuits were measured by a parameter analyzer (Keithley 4200-SCS) in DC voltage and current sweep mode, a programmable DC voltage source (Keithley 230, constant V_{DD} of 5 V), a pulse function generator (Agilent 33250A, V_{in} of 100 Hz with a repetitive rectangular waveform ranging from zero to 5 V), and an oscilloscope (Tektronix DPO3054). White LED source with a current control module (NIC-199) was used for NBTIS/PBTIS measurements. The power of the light source was ≈0.9 mW in radiometric value at 10 cm away from the source.

Finite-Element Method Simulation: The thermal diffusion simulations were calculated by COMSOL Multiphysics 4.4 using the heat transfer mode. The heat flux of a complete device was calculated by a heat transfer equation. The absorption coefficient and reflectance were measured by a UV spectrometer (Shimadzu UV 3101pc). The mesh size of an entire device structure distributed from 0.4 to 200 nm.

Supporting Information

Supporting Information is available from the Wiley Online Library or from the author.

Acknowledgements

[1] R. Azuma, Y. Baillot, R. Behringer, S. Feiner, S. Julier, B. MacIntyre, *IEEE Comput. Graphics Appl.* **2001**, *21*, 34.

[2] Z. L. Wang, *Adv. Mater.* **2012**, *24*, 280.

[3] S. Kim, S. Kim, J. Park, S. Ju, S. Mohammadi, *ACS Nano* **2010**, *4*, 2994.

[4] D. Jin, T. Kim, H. Koo, D. Stryakhilev, H. Kim, S. Seo, M. Kim, H. Min, H. Chung, S. Kim, *SID Symp. Dig. Tech. Pap.* **2010**, *41*, 703.

[5] R.-Q. Ma, K. Rajan, M. Hack, J. J. Brown, J. H. Cheon, S. H. Kim, M. H. Kang, W. G. Lee, J. Jang, *SID Symp. Dig. Tech. Pap.* **2008**, *39*, 425.

[6] K. K. Banger, Y. Yamashita, K. Mori, R. L. Peterson, T. Leedham, J. Rickard, H. Sirringhaus, *Nat. Mater.* **2011**, *10*, 45.

[7] K. Nomura, H. Ohta, A. Takagi, T. Kamiya, M. Hirano, H. Hosono, *Nature* **2004**, *432*, 488.

[8] D. H. Lee, Y. J. Chang, G. S. Herman, C. H. Chang, *Adv. Mater.* **2007**, *19*, 843.

[9] T. Rembert, C. Battaglia, A. Anders, A. Javey, *Adv. Mater.* **2015**, *27*, 6090.

[10] Y. Choi, W. Park, M. S. Kang, G. Yi, J. Lee, Y. Kim, J. H. Cho, *ACS Nano* **2015**, *9*, 4288.

[11] J.-W. Jo, J. Kim, K.-T. Kim, J.-G. Kang, M.-G. Kim, K.-H. Kim, H. Ko, J. Kim, Y.-H. Kim, S. K. Park, *Adv. Mater.* **2015**, *27*, 1182.

[12] X. Liu, C. Wang, B. Cai, X. Xiao, S. Guo, Z. Fan, J. Li, X. Duan, L. Liao, *Nano Lett.* **2012**, *12*, 3596.

[13] M. C. McAlpine, H. Ahmad, D. Wang, J. R. Heath, *Nat. Mater.* **2007**, *6*, 379.

[14] J. Jang, *Mater. Today* **2006**, *9*, 46.

[15] S. Kim, J. H. Son, S. H. Lee, B. K. You, K.-I. Park, H. K. Lee, M. Byun, K. J. Lee, *Adv. Mater.* **2014**, *26*, 7480.

[16] Y. Hattori, L. Falgout, W. Lee, S.-Y. Jung, E. Poon, J. W. Lee, I. Na, A. Geisler, D. Sadhwani, Y. Zhang, Y. Su, X. Wang, Z. Liu, J. Xia, H. Cheng, R. C. Webb, A. P. Bonifas, P. Won, J.-W. Jeong, K.-I. Jang, Y. M. Song, B. Nardone, M. Nodzenski, J. A. Fan, Y. Huang, D. P. West, A. S. Paller, M. Alam, W.-H. Yeo, J. A. Rogers, *Adv. Healthcare Mater.* **2014**, *3*, 1597.

[17] R. C. Webb, A. P. Bonifas, A. Behnaz, Y. Zhang, K. J. Yu, H. Cheng, M. Shi, Z. Bian, Z. Liu, Y.-S. Kim, W.-H. Yeo, J. S. Park, J. Song, Y. Li, Y. Huang, A. M. Gorbach, J. A. Rogers, *Nat. Mater.* **2013**, *12*, 938.

[18] M. Kaltenbrunner, T. Sekitani, J. Reeder, T. Yokota, K. Kuribara, T. Tokuhara, M. Drack, R. Schwödiauer, I. Graz, S. Bauer-Gogonea, S. Bauer, T. Someya, *Nature* **2013**, *499*, 458.

[19] B. Xu, A. Akhtar, Y. Liu, H. Chen, W.-H. Yeo, S. I. Park, B. Boyce, H. Kim, J. Yu, H.-Y. Lai, S. Jung, Y. Zhou, J. Kim, S. Cho, Y. Huang, T. Bretl, J. A. Rogers, *Adv. Mater.* **2016**, *28*, 4563.

FULL PAPER

[20] X. Huang, Y. Liu, H. Cheng, W. J. Shin, J. A. Fan, Z. Liu, C. J. Lu, G. W. Kong, K. Chen, D. Patnaik, S. H. Lee, S. Hage-Ali, Y. Huang, J. A. Rogers, *Adv. Funct. Mater.* **2014**, *24*, 3846.

[21] W. H. Yeo, Y. S. Kim, J. Lee, A. Ameen, L. Shi, M. Li, S. Wang, R. Ma, S. H. Jin, Z. Kang, Y. Huang, J. A. Rogers, *Adv. Mater.* **2013**, *25*, 2773.

[22] B. Chen, T. Chang, Y. Hung, T. Hsieh, M. Tsai, P.-Y. Liao, B.-Y. Chen, Y.-H. Tu, Y.-Y. Lin, W.-W. Tsai, J.-Y. Yan, *Appl. Phys. Lett.* **2015**, *106*, 183503.

[23] H. S. Lee, J. Chung, G.-T. Hwang, C. K. Jeong, Y. Jung, J.-H. Kwak, H. Kang, M. Byun, W. D. Kim, S. Hur, S.-H. Oh, K. J. Lee, *Adv. Funct. Mater.* **2014**, *24*, 6914.

[24] C. K. Jeong, K.-I. Park, J. H. Son, G.-T. Hwang, S. H. Lee, D. Y. Park, H. E. Lee, H. K. Lee, M. Byun, K. J. Lee, *Energy Environ. Sci.* **2014**, *7*, 4035.

[25] K.-I. Park, J. H. Son, G.-T. Hwang, C. K. Jeong, J. Ryu, M. Koo, I. Choi, S. H. Lee, M. Byun, Z. L. Wang, K. J. Lee, *Adv. Mater.* **2014**, *26*, 2514.

[26] T. Ueda, M. Ishida, M. Yuri, *Jpn. J. Appl. Phys.* **2011**, *50*, 041001.

[27] K.-Y. Li, N.-H. Tai, I.-N. Lin, *Integr. Ferroelectr.* **2005**, *69*, 135.

[28] A. Pecora, L. Maiolo, M. Cuscunà, D. Simeone, A. Minotti, L. Mariucci, G. Fortunato, *Solid-State Electron.* **2008**, *52*, 348.

[29] S. Inoue, S. Utsunomiya, T. Saeki, T. Shimoda, *IEEE Trans. Electron Devices* **2002**, *49*, 1353.

[30] P. R. Tavernier, D. R. Clarke, *J. Appl. Phys.* **2001**, *89*, 1527.

[31] H. Wang, F. Lusquiños, Y. Lawrence Yao, *Appl. Phys. A: Mater. Sci. Process.* **2012**, *107*, 307.

[32] W. Li, S. Varlamov, J. Huang, *Thin Solid Films* **2015**, *576*, 42.

[33] H. Uhm, S. Lee, W. Kim, J. Park, *IEEE Electron Device Lett.* **2012**, *33*, 543.

[34] T. Rembert, C. Battaglia, A. Anders, A. Javey, *Adv. Mater.* **2015**, *27*, 6090.

[35] B. Wang, X. Yu, P. Guo, W. Huang, L. Zeng, N. Zhou, L. Chi, M. J. Bedzyk, R. P. H. Chang, T. J. Marks, A. Facchetti, *Adv. Electron. Mater.* **2016**, *2*, 1500427.

[36] X. Yu, L. Zeng, N. Zhou, P. Guo, F. Shi, D. B. Buchholz, Q. Ma, J. Yu, V. P. Dravid, R. P. H. Chang, M. Bedzyk, T. J. Marks, A. Facchetti, *Adv. Mater.* **2015**, *27*, 2390.

[37] H. Kawazoe, M. Yasukawa, H. Hyodo, M. Kurita, H. Yanagi, H. Hosono, *Nature* **1997**, *389*, 939.

[38] S. Park, K.-H. Kim, J.-W. Jo, S. Sung, K.-T. Kim, W.-J. Lee, J. Kim, H. J. Kim, G.-R. Yi, Y.-H. Kim, M.-H. Yoon, S. K. Park, *Adv. Funct. Mater.* **2015**, *25*, 2807.

[39] P.-T. Liu, Y.-T. Chou, L.-F. Teng, *Appl. Phys. Lett.* **2009**, *95*, 233504.

[40] H. Godo, D. Kawae, S. Yoshitomi, T. Sasaki, S. Ito, H. Ohara, A. Miyanaga, S. Yamazaki, *SID Symp. Dig. Tech. Pap.* **2009**, *40*, 1110.

[41] J. S. Park, T. S. Kim, K. S. Son, K. H. Lee, W. J. Maeng, H. S. Kim, E. S. Kim, K. B. Park, J. B. Seon, W. Choi, M. K. Ryu, S. Y. Lee, *Appl. Phys. Lett.* **2010**, *96*, 2.

[42] T.-C. Chen, T.-C. Chang, C.-T. Tsai, T.-Y. Hsieh, S.-C. Chen, C.-S. Lin, M.-C. Hung, C.-H. Tu, J.-J. Chang, P.-L. Chen, *Appl. Phys. Lett.* **2010**, *97*, 112104.

[43] K. Kaftanoglu, S. Member, S. M. Venugopal, M. Marrs, A. Dey, E. J. Bawolek, D. R. Allee, S. Member, D. Loy, *J. Disp. Technol.* **2011**, *7*, 339.

[44] S. H. Cho, M. K. Ryu, H.-O. Kim, O.-S. Kwon, E.-S. Park, Y.-S. Roh, C.-S. Hwang, S.-H. K. Park, *Phys. Status Solidi* **2014**, *211*, 2126.

[45] Y. G. Mo, M. Kim, C. K. Kang, J. H. Jeong, Y. S. Park, C. G. Choi, H. D. Kim, S. S. Kim, *J. Soc. Inf. Disp.* **2011**, *19*, 16.

[46] H.-S. Kim, K.-B. Park, K. S. Son, J. S. Park, W.-J. Maeng, T. S. Kim, K.-H. Lee, E. S. Kim, J. Lee, J. Suh, J.-B. Seon, M. K. Ryu, S. Y. Lee, K. Lee, S. Im, *Appl. Phys. Lett.* **2010**, *97*, 102103.

[47] J. Kim, S. Leksikov, P. Thamjamrassri, U. Lee, H. Suk, presented at *Proc. 17th Int. Conf. Human-Computer Interact. with Mob. Devices Serv.–MobileHCl'15*, New York, NY, USA, **2015**.

[48] C. Lee, G. Seo, S. Baek, presented at *The 6th Int. Conf. Information, Intell. Syst. Appl. (IISA)*, Ionian University, Corfu, Greece, **2015**.

[49] S.-Y. Huang, T.-C. Chang, M.-C. Yang, L.-W. Lin, M. Wu, K.-H. Yang, M.-C. Chen, Y.-J. Chiu, B.-L. Yeh, *Appl. Phys. Lett.* **2012**, *101*, 253502.

[50] J. H. Kim, U. K. Kim, Y. J. Chung, C. S. Hwang, *Appl. Phys. Lett.* **2011**, *98*, 232102.

[51] H. Oh, S.-M. Yoon, M. K. Ryu, C.-S. Hwang, S. Yang, S.-H. K. Park, *Appl. Phys. Lett.* **2010**, *97*, 183502.

[52] D. Luo, H. Xu, M. Zhao, M. Li, M. Xu, J. Zou, H. Tao, L. Wang, J. Peng, *ACS Appl. Mater. Interfaces* **2015**, *7*, 3633.

[53] J.-Y. Kwon, J. S. Jung, K. S. Son, K.-H. Lee, J. S. Park, T. S. Kim, J.-S. Park, R. Choi, J. K. Jeong, B. Koo, S. Lee, *J. Electrochem. Soc.* **2011**, *158*, H433.

[54] J.-H. Jeon, Y. H. Hwang, B.-S. Bae, *Electrochem. Solid-State Lett.* **2012**, *15*, H123.

[55] H.-S. Kim, J. S. Park, H.-K. Jeong, K. S. Son, T. S. Kim, J.-B. Seon, E. Lee, J. G. Chung, D. H. Kim, M. Ryu, S. Y. Lee, *ACS Appl. Mater. Interfaces* **2012**, *4*, 5416.

[56] S. Il Park, A. P. Le, J. Wu, Y. Huang, X. Li, J. A. Rogers, *Adv. Mater.* **2010**, *22*, 3062.

[57] Y. Sun, W. M. Choi, H. Jiang, Y. Y. Huang, J. A. Rogers, *Nat. Nanotechnol.* **2006**, *1*, 201.

[58] J. A. Rogers, T. Someya, Y. Huang, *Science* **2010**, *327*, 1603.

[59] H. Li, Q. Zhao, W. Wang, H. Dong, D. Xu, G. Zou, H. Duan, D. Yu, *Nano Lett.* **2013**, *13*, 1271.

[60] P. H. Lau, K. Takei, C. Wang, Y. Ju, J. Kim, Z. Yu, T. Takahashi, G. Cho, A. Javey, *Nano Lett.* **2013**, *13*, 3864.

[61] M. Herrmann, N. Fruehauf, *SID Symp. Dig. Tech. Pap.* **2014**, *45*, 476.

[62] D. Han Kang, J. Ung Han, M. Mativenga, S. Hwa Ha, J. Jang, *Appl. Phys. Lett.* **2013**, *102*, 083508.

[63] A. Dey, A. Indluru, S. M. Venugopal, D. R. Allee, T. L. Alford, *IEEE Electron Device Lett.* **2010**, *31*, 1416.

[64] I. T. Cho, J. W. Lee, J. M. Park, W. S. Cheong, C. S. Hwang, J. S. Kwak, I. H. Cho, H. I. Kwon, H. Shin, B. G. Park, J. H. Lee, *IEEE Electron Device Lett.* **2012**, *33*, 1726.